

next) generation of X-ray spectrometers by more than an order of magnitude in spectral resolution. Such improved capability has enabled us to obtain a ground-based measurement of the kinetic temperature and turbulent velocity of a coronal ion. The observed good agreement between the observed and expected wavelengths of the Ti II and Fe XIII lines indicates that the chromosphere and the corona of CN Leo are not in relative motion with respect to each other as expected for a quiescent corona. CN Leo is a flare star—albeit not flaring (at least in a major way) during our UVES observations. During a flare mass motions must occur, possibly with speeds of up to a few hundred kilometres per second. A line-of-sight velocity of 100 km s^{-1} would lead to a 1.13 \AA shift of the Fe XIII line, which should be easily detectable with UVES. Thus it should be possible to directly diagnose the coronal dynamics of flares on CN Leo and other stars.

It is a challenge to extend coronal line observations to a larger sample of stars, and to stars of earlier spectral type. With such samples, ground-based searches for stellar coronal activity cycles—similar to those on the Sun—could be carried out. For sufficiently rapid rotators, Doppler tomography could be used to study stellar coronal structure. With yet deeper exposures, it should be possible to detect weaker coronal lines (for example, Ca XII at $3,329 \text{ \AA}$), and interesting plasma diagnostics would be obtained by extending the coronal line observations to $5,403 \text{ \AA}$ (Fe XIV), $6,374 \text{ \AA}$ (Fe X), and $10,796$ and $10,747 \text{ \AA}$ (Fe XIII). As the photospheric background is much stronger at longer wavelengths, this will be a challenge both for observations and atmospheric modelling. □

Received 2 May; accepted 18 May 2001.

1. Linsky, J. L. Non radiative activity across the H-R diagram—Which types of stars are solar-like? *Sol. Phys.* **100**, 333–362 (1985).
2. Schmitt, J. H. M. M. Coronae on solar-like stars. *Astron. Astrophys.* **318**, 215–230 (1997).
3. Grottian, W. Zur Frage der Deutung der Linien im Spektrum der Sonnenkorona. *Naturwissenschaften* **27**, 214 (1939).
4. Edlén, B. Die Deutung der Emissionslinien im Spektrum der Sonnenkorona. *Z. Astrophys.* **22**, 30–62 (1942).
5. Taylor, A. R. & Paredes, J. M. (eds) *Radio Emission from the Stars and the Sun* (ASP Conf. Ser. 93, Astronomical Society of the Pacific, San Francisco, 1996).
6. Vaiana, G. S. *et al.* Results from an extensive Einstein stellar survey. *Astrophys. J.* **244**, 163–182 (1981).
7. Guillout, P. *et al.* The stellar content of soft X-ray surveys. II. Cross-correlation of the ROSAT All-Sky Survey with the Tycho and Hipparcos catalogs. *Astron. Astrophys.* **351**, 1003–1015 (1999).
8. Linsky, J. L., Wood, B. E., Brown, A. & Osten, R. A. Dissecting Capella's corona: GHRS spectra of the Fe XXI 1354 and He II λ 1640 lines from each of the capella stars. *Astrophys. J.* **492**, 767–777 (1998).
9. Wallerstein, G., Böhm, K. H. & Oke, J. B. in *Extreme Ultraviolet Astronomy* (eds Malina, R. F. & Bowyer, S.) 113 (Pergamon, New York, 1991).
10. D'Odorico, S., Kaper, L. & Kaufer, A. *VLT UVES Manual* at (<http://www.eso.org/instruments/uves/userman/>) (2000).
11. Robinson, R. D., Carpenter, K. G., Percival, J. W. & Bookbinder, J. A. A search for microflaring activity on dMe flare stars. I. Observations of the dM8e star CN Leonis. *Astrophys. J.* **451**, 795–805 (1995).
12. Barbera, M., Micela, G., Sciortino, S., Harnden, F. R. Jr & Rosner, R. X-ray emission at the low-mass end—Results from an extensive Einstein Observatory survey. *Astrophys. J.* **414**, 846–866 (1993).
13. Schmitt, J. H. M. M., Fleming, T. A. & Giampapa, M. S. The X-ray view of the low-mass stars in the solar neighborhood. *Astrophys. J.* **450**, 392–400 (1995).
14. Arnaud, M. & Raymond, J. Iron ionization and recombination rates and ionization equilibrium. *Astrophys. J.* **398**, 394–406 (1992).
15. Flower, D. R. & Pineau Des Forets, G. Excitation of the Fe XIII spectrum in the solar corona. *Astron. Astrophys.* **24**, 181–192 (1973).
16. Harris, D. E. *et al.* *The Einstein Observatory Catalog of IPC X-ray Sources*, Vol. 4 (Smithsonian Astrophysical Observatory, Cambridge, Massachusetts, 1990).
17. Cheng, C., Doschek, G. A. & Feldman, U. The dynamical properties of the solar corona from intensities and emission line widths of EUV forbidden lines. *Astrophys. J.* **227**, 1037–1046 (1979).
18. Chae, J., Schühle, U. & Lemaire, P. SUMER measurements of non thermal motions: Constraints on coronal heating mechanisms. *Astrophys. J.* **505**, 957–973 (1998).

Acknowledgements

The data reported in this paper were collected at ESO's Paranal Observatory. We gratefully acknowledge the support of the ESO staff. We also thank D. Flower for discussions on Fe XIII.

Correspondence and requests for materials should be addressed to J.H.M.M.S. (e-mail: jschmitt@hs.uni-hamburg.de).

Evidence for ubiquitous strong electron–phonon coupling in high-temperature superconductors

A. Lanzara^{*†}, P. V. Bogdanov^{*}, X. J. Zhou^{*}, S. A. Kellar^{*}, D. L. Feng^{*}, E. D. Lu[†], T. Yoshida[‡], H. Eisaki^{*}, A. Fujimori[‡], K. Kishio[§], J.-I. Shimoyama[§], T. Noda^{||}, S. Uchida^{||}, Z. Hussain[†] & Z.-X. Shen^{*}

^{*} Department of Physics, Applied Physics and Stanford Synchrotron Radiation Laboratory, Stanford University, Stanford, California 94305, USA

[†] Advanced Light Source, Lawrence Berkeley National Laboratory, Berkeley, California 94720, USA

[‡] Department of Physics; and [§] Department of Applied Chemistry, University of Tokyo, Bunkyo-ku, Tokyo 113-8656, Japan

^{||} Department of Superconductivity, University of Tokyo, Yayoi 2-11-16, Bunkyo-ku, Tokyo 133, Japan

Coupling between electrons and phonons (lattice vibrations) drives the formation of the electron pairs responsible for conventional superconductivity¹. The lack of direct evidence for electron–phonon coupling in the electron dynamics of the high-transition-temperature superconductors has driven an intensive search for an alternative mechanism. A coupling of an electron with a phonon would result in an abrupt change of its velocity and scattering rate near the phonon energy. Here we use angle-resolved photoemission spectroscopy to probe electron dynamics—velocity and scattering rate—for three different families of copper oxide superconductors. We see in all of these materials an abrupt change of electron velocity at 50–80 meV, which we cannot explain by any known process other than to invoke coupling with the phonons associated with the movement of the oxygen atoms. This suggests that electron–phonon coupling strongly influences the electron dynamics in the high-temperature superconductors, and must therefore be included in any microscopic theory of superconductivity.

We investigated the electronic quasiparticle dispersions in three different families of hole-doped copper oxides: $\text{Bi}_2\text{Sr}_2\text{CaCu}_2\text{O}_8$ (Bi2212) and Pb-doped Bi2212 (Pb-Bi2212), Pb-doped $\text{Bi}_2\text{Sr}_2\text{CuO}_6$ (Pb-Bi2201) and $\text{La}_{2-x}\text{Sr}_x\text{CuO}_4$ (LSCO). Except for the Bi2201 (overdoped, transition temperature $T_c = 7 \text{ K}$) data and that in Fig. 3b, recorded at beam-line 5.4 of the Stanford Synchrotron Radiation Laboratory (SSRL), all the data were recorded at the Advanced Light Source (ALS), as detailed elsewhere².

The top panels of Fig. 1 report the dispersions—derived from the momentum distribution curves, MDCs—along the $(0, 0) - (\pi, \pi)$ direction for LSCO (Fig. 1a) and Bi2212 (Fig. 1b) in the superconducting state, and for Pb-Bi2201 in the normal state (Fig. 1c), versus the rescaled momentum, k' . We calculate k' by normalizing to one the momentum k relative to the Fermi momentum k_F , $(k - k_F)$, at the binding energy $E = 170 \text{ meV}$. A 'kink' in the dispersion around 50–80 meV, indicated by thick arrows in the figure, is the many-body effect of interest and has been previously reported^{2–5}. The direct comparison suggests a similar phenomenon in different systems (although details differ) and at different dopings, with the effect getting stronger in the underdoped region. These results put a strong constraint on the nature of the effect. The similar energy scale of the excitation (50–80 meV) in systems with very different gap energy, ranging from 10–20 meV for LSCO and Bi2201, to 30–50 meV for Bi2212, rules out the superconducting gap as the origin. The data also rule out the proposed explanation⁶ in terms of coupling with the magnetic mode at 41 meV (ref. 7), because of its temperature dependence and its ubiquity. The phenomenon is observed in LSCO where the magnetic mode does not exist. It is also observed well above the transition temperature T_c

in all cases, but the magnetic mode sets in at T_c for optimal and overdoped samples⁷ (for example, the 30 K data from overdoped Pb-Bi2201 are measured at six times T_c). These considerations, based on direct experimental evidence, leave phonons as the only possible candidates.

The phonon interpretation receives strong support from a direct comparison between photoemission results and neutron-scattering data on LSCO. As shown by the red arrow and the shaded area in Fig. 1a, the energy of the zone boundary in-plane oxygen-stretching longitudinal optical (LO) phonon, identified by neutrons as being strongly coupled to charge^{8,9}, coincides with the 'kink' energy in our data—barring a minor correction due to the small superconducting gap of 10 meV. We identify this mode as the highest energy phonon that contributes strongly to the ARPES (angle-resolved photoemission spectroscopy) data. However, other phonon contributions should be considered as well; for example, the apical mode¹⁰, which is related to the in-plane oxygen-stretching mode. Additional support for the phonon model comes also from an analysis of temperature dependence. In the lower panels of Fig. 1 we report the evolution of the 'kink' above and below the transition temperature for LSCO (Fig. 1d) and Bi2212 (Fig. 1e). In both cases, the 'kink' clearly persists above the transition temperature as expected for electron–phonon interaction, but a thermal broadening is present.

Figure 2a–c shows data from energy distribution curves (EDCs) of Bi2212 along the $(0, 0) - (\pi, \pi)$ direction at different dopings; also shown for comparison are corresponding data for the Be (0001) surface state^{11,12} (Fig. 2d)—in which the electron–phonon interaction is known to be strong—and simulated spectra (Fig. 2e). A

strong similarity among the raw spectra can be observed. In the case of Be, the 65-meV phonon sets a scale below which a sharp quasiparticle is possible. This leads to a 'dip' or 'break' in the spectra near the phonon energy, indicated by the vertical dashed line. This feature is well reproduced in the simple simulation, where a quasiparticle is isotropically coupled to a collective mode near 70 meV (refs 6, 13). The Bi2212 data show also a clear resemblance, with a $(\pi, 0)$ LO-phonon near 55 meV (ref. 9), but pushed up by the superconducting gap. All the data suggest that there is an energy scale close to the expected phonon frequency. Therefore, the notable similarity between the Bi2212 data and that of a known phonon case strongly supports the phonon explanation.

In Fig. 3a we report the quasiparticle width of Bi2212 for different doping, obtained using a typical procedure². As shown before^{2,3}, the width decreases more rapidly below the relevant energy, which corresponds to the kink position in the dispersion. This again is consistent with the case of an electron–phonon coupled system, complementing dispersion data in Fig. 1. The drop in the scattering rate near the relevant energy is also seen in optics experiments¹⁴. Figure 3b reports the 'dip' energy of ARPES spectra near $(\pi, 0)$ as a function of doping. The data are consistent with the idea that the 55-meV LO phonon energy sets the lower bound⁹. A realistic model—which considers the change of the $(\pi, 0)$ band position with doping, bilayer splitting (which severely distorts $(\pi, 0)$ spectra^{15,16}), electron–phonon interaction and energy gap—will be needed to understand the specifics of the data, including the small decrease of the dip energy with doping.

In a simple electron–phonon model, the ratio of the velocities of the bare and the dressed electrons is $(\lambda + 1)$, where λ measures

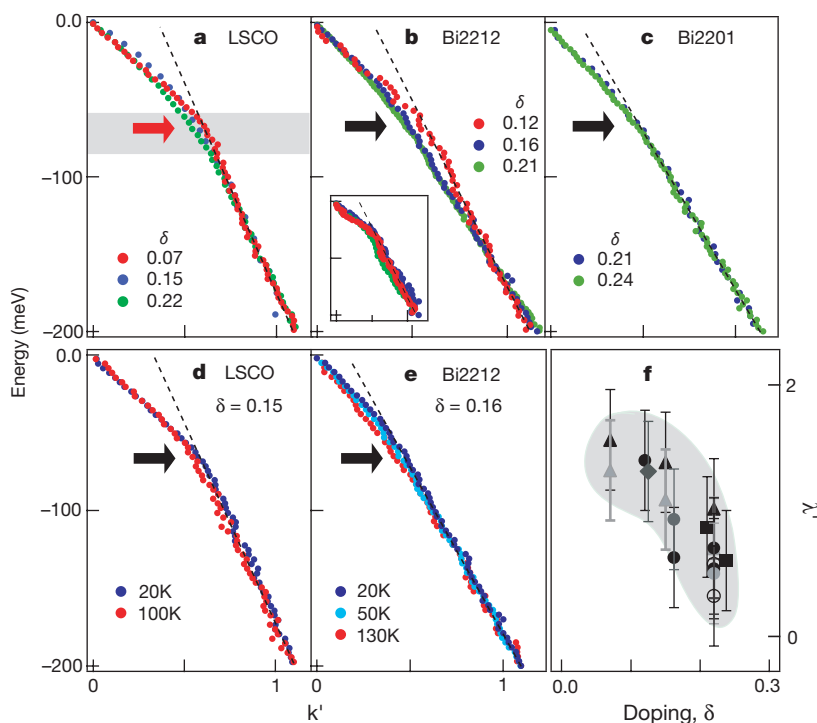


Figure 1 Ubiquity of a sudden change ('kink') in the dispersion. Top panels are plots of the dispersion (derived from the momentum distribution curves) along $(0, 0) - (\pi, \pi)$ (except panel **b** inset, which is off this line) versus the rescaled momentum K' for different samples and at different doping levels. **a–c**, Doping (δ) dependence of LSCO (at 20 K; **a**), Bi2212 (superconducting state, 20 K; **b**), and Bi2201 (normal state, 30 K; **c**). Dotted lines are guides to the eye. The kink position in **a** is compared with the phonon energy at $q = (\pi, 0)$ (thick red arrow) and the phonon width and dispersion (shaded area) from neutron data⁸. The doping was determined from the T_c versus doping universal curve. Inset in **b**, dispersions off the $(0, 0) - (\pi, \pi)$ direction, showing also a sharpening of the

kink on moving away from the nodal direction. The black arrows indicate the position of the kink in the dispersions. **d,e**, Temperature dependence of the dispersions for LSCO (**d**, optimally doped) and Bi2212 (**e**, optimally doped). **f**, Doping dependence of λ' (see text) along the $(0, 0) - (\pi, \pi)$ direction as a function of doping. Data are shown for LSCO (filled triangles) and NdLSCO (1/8 doping; filled diamonds), Bi2201 (filled squares) and Bi2212 (filled circles in the first Brillouin zone, and unfilled circles in the second zone). The different shadings represent data obtained in different experimental runs. Blue area is a guide to the eye.

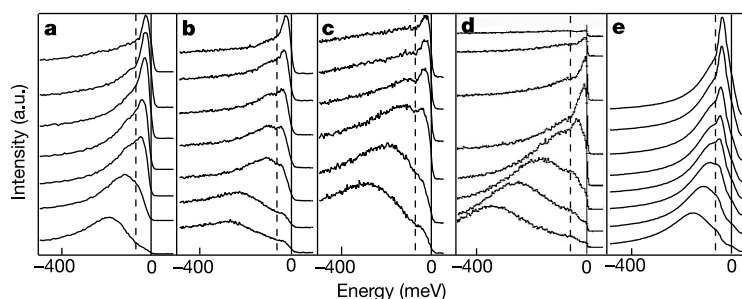


Figure 2 Double-peak features in the photoemission spectra due to strong electron–phonon interaction. **a–c**, Raw energy distribution curves (EDCs) along the $(0, 0) \rightarrow (\pi, \pi)$ direction for overdoped Pb-Bi2212 ($T_c = 70$ K; **a**), for optimally doped Bi2212 ($T_c = 91$ K; **b**) and for underdoped Bi2212 ($T_c = 84$ K; **c**). **d**, Raw EDCs for the Be(0001) surface¹¹.

e, EDCs of simulated spectra, obtained in the simple case of an isotropic coupling to a single phonon mode. The straight, vertical line highlights the zero-energy position, and a dashed line highlights the approximate ‘dip’ position, which is related to known phonon energy⁹ (see text).

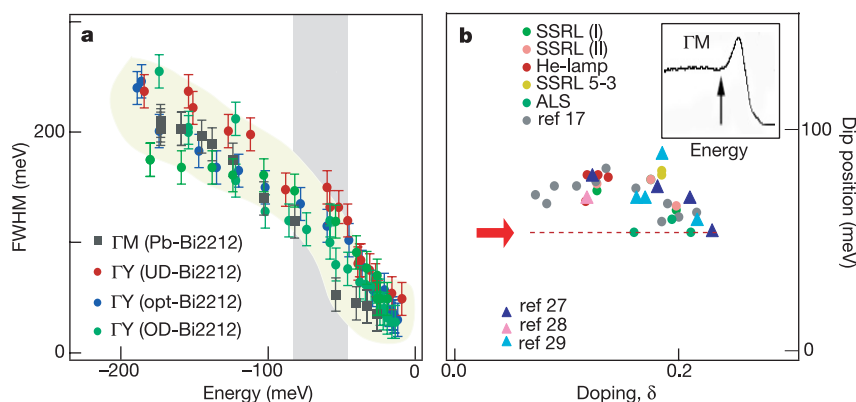


Figure 3 Comparison of the observed effect in photoemission, tunnelling and neutron data. **a**, Quasiparticle width along the ΓY direction $((0, 0) \rightarrow (\pi, \pi))$; circles) for Bi2212 and Pb-Bi2212, and along the ΓM direction $((0, 0) \rightarrow (\pi, 0))$; squares) for the superstructure-free Pb-Bi2212 system. **b**, Doping-dependence of the dip position for the Bi2212 samples, near the $(\pi, 0)$ region, as indicated in the inset of **b** by the arrow. The dip position has been obtained both from photoemission (circles) and tunnelling (triangles^{27–29}) data. The photoemission data were collected at SSRL, beamline 5.4 in

transmission mode (I) (green circles) and angular mode (II) (pink circles), and at SSRL, beamline 5.3 (yellow circles). The data at ALS were collected in angular mode (light green circles). Red circles represent the He-lamp data, collected with a Scienta analyser. Our data are compared with data points from ref. 17 (grey circles). The red arrow indicates the LO phonon energy at $(\pi, 0)$ ⁹, which sets the lower bound for the dip. FWHM, full-width at half-maximum; UD, underdoped; OD, overdoped; opt, optimum doping.

the electron–phonon coupling strength. We can extract a similar quantity from the ratio between the high-energy velocity above the phonon energy (which approximates the velocity without phonon interaction) and the dressed velocity below the phonon energy. The two velocities are determined by fitting the experimental dispersions with two straight lines. The coupling strength determined from the experimental data, λ' , is proportional to λ , but is an overestimate for two reasons. The first is that the high-energy dispersion overestimates the bare velocity. The second is that electron–electron scattering also influences the dispersion away from the phonon energy, especially in the high-energy part that we use as the bare velocity. In Fig. 1f we report the doping dependence of λ' along the (π, π) direction. An estimate of λ can alternatively be obtained by fitting the experimental data with a model (for example, the Debye model), or assuming the bare velocity as given from band calculations. In both cases the obtained values are smaller than λ' , but the decreasing trend with doping is identical.

In Fig. 4a, we show the velocity ratio for different materials as a function of the angle ϕ along the entire Fermi surface (Fig. 4b). Data obtained from different experimental runs are included in the figure (filled and unfilled symbols). In Fig. 4b we report the rescaled MDC-derived dispersions for Pb-Bi2212 taken with 55-eV photons along the two high-symmetry directions, ΓY $((0, 0) \rightarrow (\pi, \pi))$ and ΓM $((0, 0) \rightarrow (\pi, 0))$. The total change in the ratio with angle is slightly less than a factor of two. In particular, the data from both Pb-doped Bi2212 and Pb-doped Bi2201, where the superstructure effect near $(\pi, 0)$ is minimized, give confidence to the conclusion.

The conversion from velocity ratio to the coupling constant λ away from the (π, π) direction requires a correction due to the band structure effect (including bilayer-splitting) that increases away from the (π, π) direction^{15,16}, but the conclusion that the coupling is not very anisotropic remains true. No direct relation with the superconducting transition is observed, as can be seen in the same figure where data above (100 K) and below (20 K) the critical temperature are reported in the case of Pb-doped Bi2212. Both the angle dependence and the temperature dependence are consistent with the phonon interpretation, as phonons are more isotropic and will not disappear above T_c .

Although these experimental findings point toward phonons as the only possible model, some previous work needs to be addressed. The kink in the dispersion along the (π, π) direction and the dip in the EDCs near $(\pi, 0)$ has been attributed⁶ to the 41-meV magnetic mode (ref. 7). Comparing the doping dependence of the energy difference between the dip and the superconducting gap in photoemission data, with that of the magnetic mode in neutron data, a definitive proof for the magnetic mode as the origin of the ‘peak–dip–hump’ structure has been claimed¹⁷. On the other hand, the absence of an energy scale in the problem has been put forward⁴, and the kink in the dispersion has been overlooked⁴. The curving in the normal state dispersion has been attributed to the marginal Fermi liquid (MFL) self-energy¹⁸, and the presence of a sharp kink below T_c has been attributed to coupling to the (π, π) magnetic mode¹⁹.

Apart from its incompatibility with our data, the above magnetic

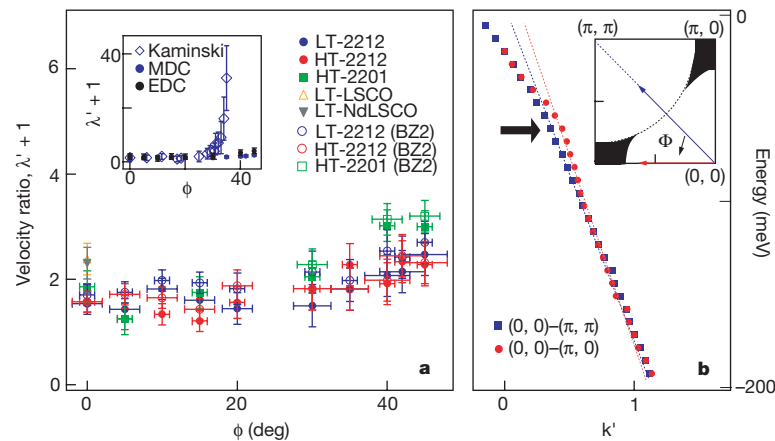


Figure 4 Momentum dependence of the velocity ratio above and below the critical temperature. The locations of the sections in the Brillouin zone are shown in the inset of **b**. ϕ is defined as the angle between the Γ –Y line and the line from Γ to the point on the Fermi surface considered. **a**, The velocity ratio versus angle ϕ along the Fermi surface. The open and filled symbols represent the values obtained fitting the MDC-derived dispersions in different experimental runs. HT and LT indicate the values of the velocity ratios obtained above and below the critical temperature. The HT data for Pb-Bi2212 were collected at 100 K (red circle) whereas the LT data were collected at 20 K (blue circle). The HT data for the Pb-Bi2201 system (squares) were collected at 30 K. The LT data (at 20 K)

mode model has serious weaknesses. First, the mode contains only a few per cent of the total spin fluctuation spectral weight²⁰, so it is an unlikely explanation for the very large change seen in EDC spectra above and below T_c . Second, the electronic model is difficult to implement self-consistently, as the mode will be altered by the interaction with electrons⁶. Third, the magnetic mode calculation claims to reproduce the experimental data that yield a huge change of the velocity ratio near the $(\pi, 0)$ region⁶. The inset of Fig. 4a compares the velocity ratio found in the present study with previous data³. The comparison shows good agreement for $\phi \leq 30^\circ$, but a large discrepancy is observed for $\phi \geq 30^\circ$. We attribute this difference to confusion caused by the superstructure, which complicates the data near the $(\pi, 0)$ region in the pure Bi2212 sample used in the previous study³. We have chosen superstructure-free Pb-Bi2212 for this investigation.

Our data and the above discussion rule out the magnetic mode as a possible model, and this also makes the ‘MFL plus magnetic mode’ interpretation an unsuitable explanation for the data. Furthermore, some of the normal-state dispersion data—for example, the 7% underdoped LSCO (Fig. 1a) measured at T_c where the kink is sharper—cannot be fitted within the MFL approach, even with an arbitrary choice of parameters. If the 7% LSCO data can only be explained by coupling to phonons, it is likely that a similar effect, observed at higher doping and temperatures, requires the same cause. Finally, this attempt to attribute the ‘kink’ in the dispersion, occurring at the same energy above and below T_c , to two different origins is not consistent with the data in Fig. 1d and e, where it can be seen that the effect washes out gradually with temperature.

The phonon model can explain all the aspects of the data attributed to the magnetic mode in a more natural way (N. Nagaosa *et al.*, personal communication). This approach has the added advantage of not suffering from the tiny spectral weight and the self-consistency issue present in the magnetic mode calculation. The phonon picture naturally explains the gradual temperature evolution observed in the MDC-derived dispersions.

Although electron–phonon interaction provides the only interpretation consistent with overall body of data, we need to mention a few caveats. The standard theory of electron–phonon coupling predicts a drop in resistivity at phonon frequency Ω , or a saturation

along the nodal direction for the LSCO and NdLSCO systems are also included (unfilled yellow and filled grey triangles). All velocity ratios are obtained for sections perpendicular to the Fermi surface at given ϕ . The inset of **a** compares the velocity ratios for Pb-Bi2212 as obtained from EDC (black filled circles) with data³ on pure Bi2212 (unfilled diamonds). In **b**, the rescaled MDC-derived dispersions, along the nodal and anti-nodal directions, are shown for the Pb-Bi2212. The small deviation above the phonon energy (indicated by the thick arrow) is caused by the difference in dispersion along the two directions, which are quite different if plotted with unscaled k .

above a temperature $T \approx (0.3 - 0.5)\Omega$. The drop at Ω has been observed and discussed in connection with the data in Fig. 3, although it was given an alternative interpretation²². The temperature dependence of the resistivity shows a complex doping dependence, with a saturation seen in the underdoped regime but not near the optimal and overdoped regimes²². An understanding of this complex behaviour requires going beyond the simple Fermi liquid theory, but is not incompatible with the presence of electron–phonon coupling²³. The lack of resistivity saturation is also seen in doped C_{60} compounds where the electron–phonon interaction is very strong²⁴. An improved theory needs to consider the strong electron–electron interaction, the pseudogap²⁵, and vertex correction, that suppress the large momentum transfer scatterings²⁶, making phonons hard to detect by resistivity experiments. Finally, we stress that electron–phonon interaction in strongly correlated materials is a largely unexplored topic, and we hope that our finding will stimulate more theoretical work. □

Received 13 February; accepted 5 June 2001.

1. Bardeen, J., Cooper, L. N. & Schrieffer, J. R. Theory of superconductivity. *Phys. Rev.* **108**, 1175–1204 (1957).
2. Bogdanov, P. V. *et al.* Evidence for an energy scale for quasiparticle dispersion in $\text{Bi}_2\text{Sr}_2\text{CaCu}_2\text{O}_{8-\delta}$. *Phys. Rev. Lett.* **85**, 2581–2584 (2000).
3. Kaminski, A. *et al.* Renormalization of spectral lineshape and dispersion below T_c in $\text{Bi}_2\text{Sr}_2\text{CaCu}_2\text{O}_{8-\delta}$. Preprint cond-mat/0004482 at (<http://xxx.lanl.gov>) (2000).
4. Valla, T. *et al.* Evidence for quantum critical behavior in the optimally doped cuprate $\text{Bi}_2\text{Sr}_2\text{CaCu}_2\text{O}_{8-\delta}$. *Science* **285**, 2110–2113 (1999).
5. Zhou, X. J. *et al.* Dual nature of the electronic structure of the stripe phase. *Phys. Rev. Lett.* **86**, 5578–5581 (2001).
6. Eschrig, M. & Norman, M. R. Neutron resonance: modeling photoemission and tunneling data in the superconducting state of $\text{Bi}_2\text{Sr}_2\text{CaCu}_2\text{O}_{8-\delta}$. *Phys. Rev. Lett.* **85**, 3261–3264 (2000).
7. He, H. *et al.* Resonant spin excitation in an overdoped high temperature superconductor. Preprint cond-mat/0002013 at (<http://xxx.lanl.gov>) (2000).
8. McQueeney, R. J. *et al.* Anomalous dispersion of LO phonons in $\text{La}_{1.85}\text{Sr}_{0.15}\text{CuO}_4$ at low temperatures. *Phys. Rev. Lett.* **82**, 628–631 (1999).
9. Petrov, Y. *et al.* Phonon signature of charge inhomogeneity in high temperature superconductors $\text{YBa}_2\text{Cu}_3\text{O}_{6+x}$. Preprint cond-mat/0003414 at (<http://xxx.lanl.gov>) (2000).
10. Bianconi, A. *et al.* Determination of local lattice distortions in the CuO_2 plane of $\text{La}_{1.85}\text{Sr}_{0.15}\text{CuO}_4$. *Phys. Rev. Lett.* **76**, 3412–3415 (1996).
11. Hengsberger, M., Purdie, D., Segovia, P., Garnier, M. & Baer, Y. Photoemission study of a strongly coupled electron-phonon system. *Phys. Rev. Lett.* **83**, 592–595 (1999).
12. Lashell, S., Jensen, E. & Balasubramanian, T. Nonquasiparticle structure in the photoemission spectra from the $\text{Be}(0001)$ surface and determination of the electron self energy. *Phys. Rev. B* **61**, 2371–2374 (2000).

13. Scalapino, D. J. in *Superconductivity* (ed. Parks, R. D.) 449 (Marcel Dekker, New York, 1969)
14. Puchkov, A. V., Basov, D. N. & Timusk, T. The pseudogap state in high T_c superconductors: An infrared study. *J. Phys. Condens. Matter* **8**, 10049–10082 (1996).
15. Feng, D. L. *et al.* Bilayer splitting in the electronic structure of heavily overdoped $\text{Bi}_2\text{Sr}_2\text{CaCu}_2\text{O}_{8+\delta}$. *Phys. Rev. Lett.* **86**, 5550–5553 (2001).
16. Chuang, Y.-D. *et al.* Doubling of the bands in overdoped $\text{Bi}_2\text{Sr}_2\text{CaCu}_2\text{O}_{8+\delta}$ —probable evidence for c-axis bilayer coupling. Preprint cond-mat/0102386 at (<http://xxx.lanl.gov>) (2000).
17. Campuzano, J. C. *et al.* Electronic spectra and their relation to the (π, π) collective mode in high- T_c superconductors. *Phys. Rev. Lett.* **83**, 3709–3712 (1999).
18. Varma, C. M., Littlewood, P. B., Schmitt-Rink, S., Abrahams, E. & Ruckenstein, A. E. Phenomenology of the normal state of Cu-O high-temperature superconductors. *Phys. Rev. Lett.* **63**, 1996–1999 (1989).
19. Johnson, P. D. *et al.* On the doping and temperature dependence of the mass enhancement observed in the cuprate Bi2212 . Preprint cond-mat/0102260 at (<http://xxx.lanl.gov>) (2001).
20. Fong, H. F. *et al.* Polarized and unpolarized neutron scattering study of the dynamic spin susceptibility in $\text{YBa}_2\text{Cu}_3\text{O}_7$. *Phys. Rev. B* **54**, 6708–6720 (1996).
21. Carbotte, J. P. *et al.* Coupling strength of charge carriers to spin fluctuations in high-temperature superconductors. *Nature* **401**, 354–356 (1996).
22. Takagi, H. *et al.* Systematic evolution of temperature-dependent resistivity in $\text{La}_{2-x}\text{Sr}_x\text{CuO}_4$. *Phys. Rev. Lett.* **69**, 2975–2978 (1992).
23. Allen, P. B. Anomalous versus conventional low energy properties of cuprate superconductors. *Comments Condens. Matter Phys.* **15**, 327–353 (1992).
24. Gunnarsson, O. Superconductivity in fullerenes. *Rev. Mod. Phys.* **69**, 575–606 (1997).
25. Batlogg, B. *et al.* Normal-state phase-diagram of $(\text{La, Sr})_2\text{CuO}_4$ from charge and spin dynamics. *Physica C* **235**, 130–133 (1994).
26. Kulić, M. L. Interplay of electron-phonon interaction and strong correlations: the possible way to high-temperature superconductivity. *Phys. Rep.* **338**, 1–264 (2000).
27. Renner, C. H. *et al.* Pseudogap precursor of the superconducting gap in under- and overdoped $\text{Bi}_2\text{Sr}_2\text{CaCu}_2\text{O}_8$. *Phys. Rev. Lett.* **80**, 149–152 (1998); Observation of the low temperature pseudogap in the vortex core of $\text{Bi}_2\text{Sr}_2\text{CaCu}_2\text{O}_8$. *Phys. Rev. Lett.* **80**, 3606–3609 (1998).
28. Cren, T. *et al.* Influence of disorder on the local density of states in high- T_c superconducting thin films. *Phys. Rev. Lett.* **84**, 147–150 (2000).
29. De Wilde, Y. *et al.* Unusual strong-effects in the tunneling spectroscopy of optimally doped and overdoped $\text{Bi}_2\text{Sr}_2\text{CaCu}_2\text{O}_8$. *Phys. Rev. Lett.* **80**, 153–156 (1998).

Acknowledgements

We thank N. Nagaosa, D. J. Scalapino, R. Laughlin, D.-H. Lee, S. Kivelson, D. Bonn, K. A. Muller, P. Allen, N. P. Armitage, A. Damascelli and F. Ronning for discussions. The work at ALS and SSRL was supported by the Department of Energy's Office of Basic Energy Science, Division of Materials Science. The Stanford work was also supported by the NSF. A.L. thanks the Istituto Nazionale Fisica della Materia (INFM) and the University of Rome "La Sapienza" for support.

Correspondence and requests for materials should be addressed to: Z.-X.S. (e-mail: zxshen@stanford.edu).

Fragile-to-strong transition and polyamorphism in the energy landscape of liquid silica

Ivan Saika-Voivod*, Peter H. Poole* & Francesco Sciortino†

* Department of Applied Mathematics, University of Western Ontario, London, Ontario N6A 5B7, Canada

† Dipartimento di Fisica and Istituto Nazionale per la Fisica della Materia, Università di Roma La Sapienza, Piazzale Aldo Moro 2, I-00185, Rome, Italy

Liquid silica is the archetypal glass former, and compounds based on silica are ubiquitous as natural and man-made amorphous materials. Liquid silica is also the extreme case of a 'strong' liquid, in that the variation of viscosity with temperature closely follows the Arrhenius law as the liquid is cooled toward its glass transition temperature^{1,2}. In contrast, most liquids are to some degree 'fragile', showing significantly faster increases in their viscosity as the glass transition temperature is approached. Recent studies^{3–6,35,36} have demonstrated the controlling influence of the potential energy hypersurface (or 'energy landscape') of the liquid on the transport properties near the glass transition. But the origin of strong liquid behaviour in terms of the energy landscape has not yet been resolved. Here we study the static

and dynamic properties of liquid silica over a wide range of temperature and density using computer simulations. The results reveal a change in the energy landscape with decreasing temperature, which underlies a transition from a fragile liquid at high temperature to a strong liquid at low temperature. We also show that a specific heat anomaly is associated with this fragile-to-strong transition, and suggest that this anomaly is related to the polyamorphic behaviour of amorphous solid silica.

In a molecular dynamics computer simulation of an equilibrium liquid, the diffusion coefficient D is readily evaluated from the particle trajectories. Like the viscosity, D is a characteristic transport property whose deviations from the Arrhenius law serve to classify a liquid as strong or fragile. The theory of Adam and Gibbs (AG)⁷ states that D is related to the configurational entropy, S_c through

$$D = D_0 \exp(-A/TS_c) \quad (1)$$

where the parameters D_0 and A are commonly assumed to be independent of temperature, T . The entropy S_c quantifies the number of distinct configurational states explored by the liquid in equilibrium. It has been suggested that these states correspond to the 'basins' of the potential energy hypersurface (PES) sampled by the liquid^{8,9}. A basin is the set of points in phase space representing configurations having the same local minimum. The local minimum configuration is termed an inherent structure (IS), and is identified in simulation by a steepest descent minimization of the potential energy.

Following the thermodynamic formalism of Stillinger and Weber⁸, we can express the internal energy of the liquid as $E = e_{IS} + E_{\text{harm}} + E_{\text{anh}}$, where e_{IS} is the average inherent structure energy and the last two terms are the average contributions to E due to thermal excitations about the IS. The term E_{harm} is the average harmonic contribution determined from a quadratic approximation to E around each inherent structure minimum, and E_{anh} is the remaining, necessarily anharmonic contribution. The harmonic and anharmonic potentials characterize the shape of the basin.

If the shape of the basins does not depend on e_{IS} (a condition

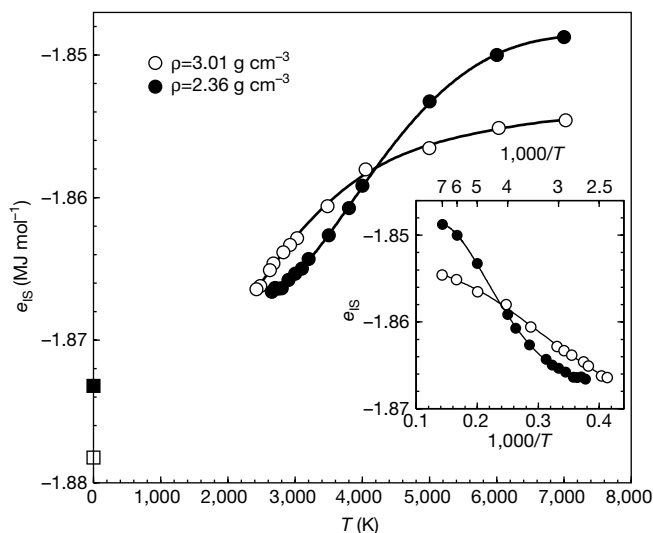


Figure 1 Variation of inherent structure energy e_{IS} with temperature T . Main panel: e_{IS} as a function of T along two isochores. At $T = 0$ we show the energy E_0 of the crystalline system at density $\rho = 2.36 \text{ g cm}^{-3}$ (filled square) and $\rho = 3.01 \text{ g cm}^{-3}$ (open square). E_0 is found by calculating the volume dependence of the potential energy at $T = 0$ of three crystal polymorphs of silica (stishovite, coesite and quartz), and then using the common tangent construction to determine the potential energy of the heterophase of coexisting crystals that would be the ground state at the required bulk value of ρ . Inset: e_{IS} for the same isochores as in the main panel, plotted as a function of $1/T$. Only the high-density data show a clear $1/T$ behaviour at low T .